Analysis of the screw feeding process in powder-based additive friction stir deposition

Wenguang Nan [a,b,*], Wenbin Xuan [a], Ziming He [a], Haimeng Hou [a], Zhonggang Sun [c], Wenya Li [d,e]

[a] School of Mechanical and Power Engineering, Nanjing Tech University, Nanjing 211816, China
[b] Faculty of physics and engineering, University of Leeds, Leeds, UK
[c] College of Materials Science and Engineering, Nanjing Tech University, Nanjing 211816, China
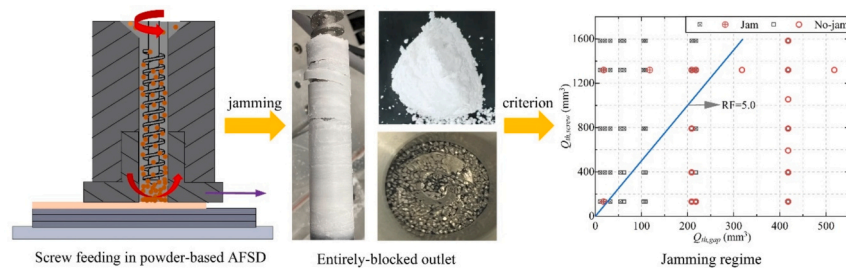[d] State Key Laboratory of Solidification Processing, School of Materials Science and Engineering, Northwestern Polytechnical University, Xi'an 710072, China
[e] Shaanxi Key Laboratory of Friction Welding Technologies, School of Materials Science and Engineering, Northwestern Polytechnical University, Xi'an 710072, China

HIGHLIGHTS

- Screw feeding in powder-based additive friction stir deposition is explored.
- Jamming makes funnel outlet entirely blocked and produces huge force on the screw.
- A mathematical model is proposed to predict critical rotational speed for jamming.
- A contracting outlet of the funnel would make the jamming problem more serious.
- Feeding rate depends on the rotational and translational speeds and the gap size.

GRAPHICAL ABSTRACT

ARTICLE INFO

ABSTRACT

The screw-feeding process in powder-based additive friction stir deposition (AFSD) is analysed in this work, in which the effect of feeding conditions on the choking/jamming problem and the feeding rate is explored through experiment and numerical simulation using Discrete Element Method (DEM). The results show that a narrow gap between the funnel outlet and the base is prone to particle jamming, which would entirely block the funnel outlet and produce a huge force on the screw. Jamming is more easily to occur when the rotational speed is relatively larger than the translational speed, and a mathematical model of the critical rotational speed above which the particle jamming and blockage would occur is proposed. Jamming is also sensitive to the design of the funnel outlet, in which a contracting outlet would make the choking and jamming problem more serious. For the feeding conditions without jamming, the feeding rate not only depends on the rotational speed of the screw but also is significantly affected by the translational speed. The feeding rate is linear to the rotational speed only when it is larger than a critical value, and this critical rotational speed increases with translational speed. The results also clarify that a good understanding of the screw-feeding process is essential for powder-based AFSD, in which an example of successful manufacturing of a 3D part is briefly illustrated in this work.

1. Introduction

Additive friction stir deposition (AFSD) has been widely explored in a wide range of applications, especially metal waste recycling [1] and damage repairing [2,3], as reviewed by Mukhopadhyay et al. [4] and Mishra et al. [5]. In this method, a rotating tool plastically deforms the material and deposits it onto a substrate, building parts layer by layer without reaching the melting point, in which the heat used to soften the material is only attributed to the intense friction and stir effects of the tool against the material or the layer. As a novel solid-state additive manufacturing technology, AFSD is able to create a fully dense build with high structural performance [6–9], such as a refined microstructure, while avoiding defects such as hot-cracking and porosity associated with fusion-based AM approaches [6,7]. In AFSD, the feed materials could range from rods [8–10] and wires [11] to chips [1,12] and powder [13,14]. Compared to rod-based AFSD, as shown in Fig. 1(a), in wires/chips/powder-based AFSD, the material could be continuously fed without any break, as shown in Fig. 1(b), and the fabricating of functionally graded structures in engineering applications could be realised. Meanwhile, compared to other methods, the material in chips/powder-based AFSD does not have restrictive requirements on the shape and size like the rods and wires, and the cheap chips collected from the machine manufacturing process or the commercial powder already available in the industry could be all used. However, minor research work is available for the chips/powder-based AFSD.

In the chips-based AFSD, a screw or an auger is usually used to consolidate the chips and force them to flow through a hollow high-speed rotating tool on a substrate and subsequent layers. Jordon et al. [1] proposed an AFSD system to recycle machine chips, which have a length of 2–3 mm, as cut from aluminium alloy 5083 plates using a mill machine, and they demonstrated that it could produce fully dense depositions with refined microstructure, and reclaim machine chips into components or repairs while maintaining high mechanical performance requirements as reported by their recent work [12]. The concept of chips-based AFSD is also extended to the friction-forging system for manufacturing tubular components, as reported by Derazkola et al. [15,16], and the friction screw extrusion system, as reported by Bor et al. [17]. It should be noted that in chips-based AFSD, the material is already plastically deformed from chips into a semi-solid state under the action of the screw before being further processed by the rotating tool. However, in powder-based AFSD, it is usually very difficult to consolidate the powder only by the screw, especially for fine powder with a size of less than 1 mm. Instead of using a screw to feed powder, Mukhopadhyay [13] directly used a compressor and duct to continuously feed powder from a container to the working zone, in which the powder was poured externally in front of the tool instead of feeding through the hollow tool, and 50–300 μm pure aluminium powder was used in their experiment. They claimed that this feeding method could mitigate the choking of the exit of the hole of the hollow tool caused by the consolidation of powder produced by the screw. Chaudhary et al. [14] used pressurized carrier gas to continuously feed the material onto the substrate through the hollow tool, which had a hole of 3 mm diameter for powder flow. To avoid blocking the small hole of the hollow tool, very fine powder was used in the experiment, i.e. 40–100 μm 6061 Al alloy powder with an average particle size of around 60 μm. Although almost no research work uses the screw-feeding technology in powder-based AFSD, it has more advantages than the gravity-discharging method in Mukhopadhyay [13] and the gas-feeding method in Chaudhary et al. [14], such as producing a more dense flow of particles, the ability to feed very fine and cohesive powder, better control of the feeding rate, et al. The main challenge in the screw-feeding process in powder-based AFSD is the particle choking/jamming problem, which blocks the exit of the hole of the rotating hollow tool, resulting in the failure of the following deposition. Meanwhile, the feeding rate is a complex function of the rotational speed of the screw, resulting in significant challenges in controlling the feeding rate and the following manufacturing process. On the other hand, compared to traditional powder screw conveying systems, there is a significant wall effect at the outlet of the screw feeding system in AFSD, i.e. the outlet is constrained by a wall close to it, making the conventional theory of screw feeding not applicable anymore. However, till now, almost no work has addressed these problems.

In this work, the jamming problem and feeding rate in the screw-feeding process in powder-based AFSD are focused, in which the screw is only used to feed powder while the friction-induced heat and plastic deformation of particles is mainly contributed by the high-speed rotating tool, as shown in Fig. 1(b2). To explore the fundamentals of the screw-feeding process, the rotation effect of the tool is omitted for simplification, and the feeding system is simplified as a screw surrounded by a funnel, and they move together and forward at a constant speed, in which the powder is fed out of the funnel by the rotating screw. The effects of the size of the gap between the funnel bottom and the base, the rotational speed of the screw, and the translational moving speed, on the feeding process are investigated through experiment and numerical simulation using Discrete Element Method (DEM). The particle jamming problem, which should be avoided in the manufacturing process, and the mass flow rate, which is essential for the good control of the quality of manufactured product, are analysed, in which the criterion of particle jamming and the principle of the variation of mass flow rate with the feeding conditions are proposed. The results will have a notable impact on the further understanding of the screw-feeding process and the development of powder-based AFSD.
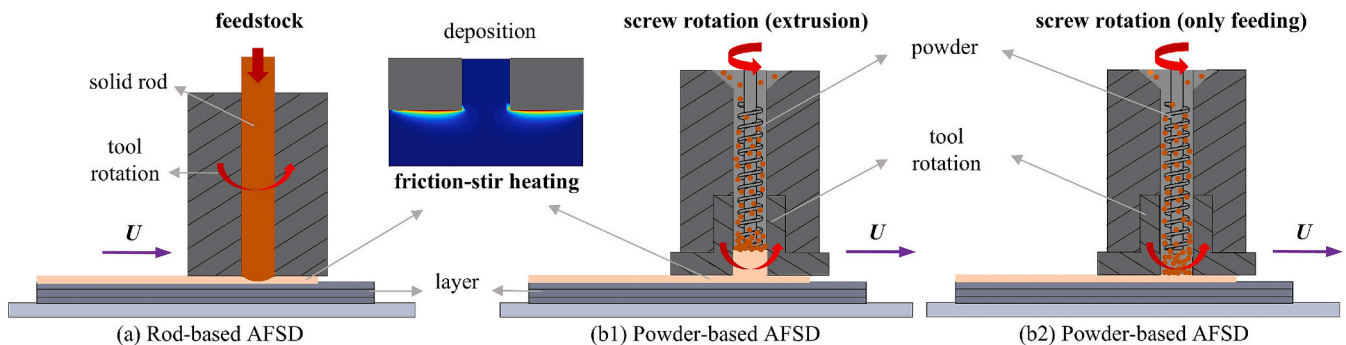

Fig. 1. Schematics of the additive friction stir deposition with the feeding materials of (a) solid rod and (b) powder, for the latter the screw could be used to (b1) severely plastically deform the powder and extrude it out the funnel in a semi-fluid state, or (b2) only used to feed the powder into the region underneath it, with following friction-induced heat and plastic deformation of particles contributed from the high-speed rotating tool.
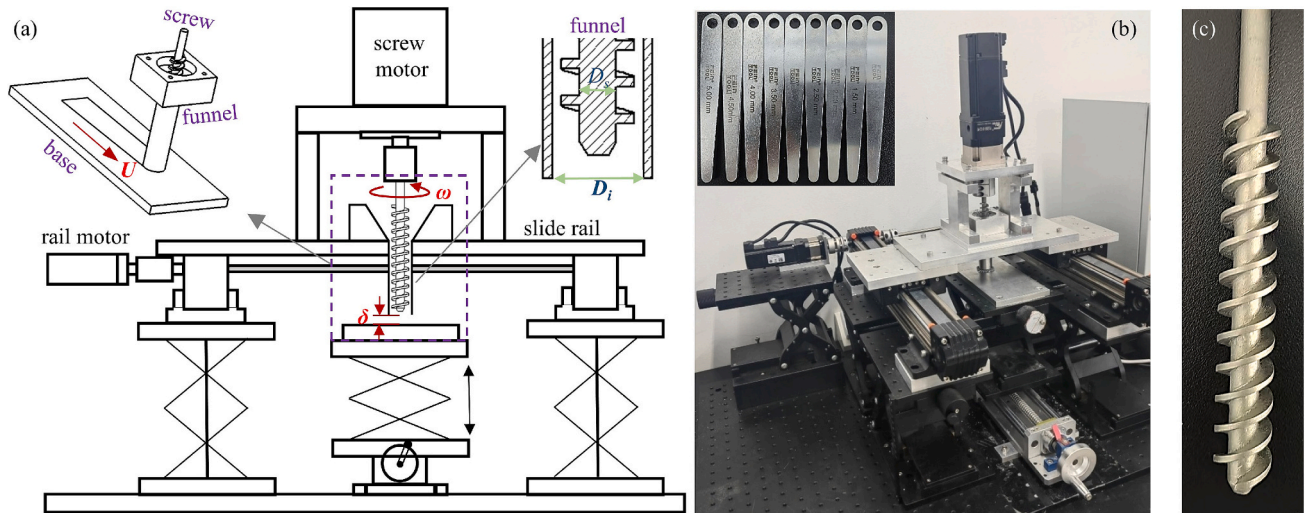
Fig. 2. Set-up of the experiment: (a) schematics of the experiment system; (b) snapshots of the experiment system with feeler gauge used in the laboratory; (c) snapshots of the screw used in the experiment.

2. Methods

2.1. Set-up of experiment system

2.1.1. Experimental system

The experimental system mainly consists of a screw, a funnel, a baseplate, and other accessories shown in Fig. 2(a)-(b). The screw and funnel are fixed on a platform with two linear slide rails, and their motion, such as the translational speed U of the supporting platform and the rotational speed ω of the screw, is controlled by the servo motors (ASD-A2, Delta Electronics Inc., China). The base is an aluminium 7075 alloy plate. To achieve convenient handling of powder before and after the experiment, the base is fixed on a linear slide rail, and thus, it could be easily moved into the region underneath the funnel for the experiment or out to open space for powder sampling after the experiment. The size of the gap between the bottom of the funnel and the top surface of the base, δ, is precisely controlled by a lift platform with a micrometre calliper, and it is further calibrated by a series of standard feeler gauges with snapshots shown in Fig. 2(b). The inner diameter of the funnel is D_i = 20 mm. A snapshot of the screw is shown in Fig. 2(c), in which the diameter of the blade and shaft is D_b = 16 mm and D_s = 8 mm, respectively.

Before the experiment, the gap size δ is set to the specified value, and the powder is fed into the top part of the funnel by using a micro-vibration feeder. Afterwards, the screw begins to rotate anti-clockwise at a constant speed ω, and the platform supporting the screw and funnel begins to move forward at a constant speed U. Therefore, the powder is forced to flow through the gap, and then it is deposited onto the base. Finally, the image of the powder layer is obtained by a CCD camera, and the mass of the powder layer is measured by a balance with a precision of 0.01 g. To minimise the effect of the start and stop of the screw motion on the results, only the mass of the powder layer located in the specified regions is used, in which the powder in other regions is carefully removed by using a thin ruler and a small brush. The specified region has

a length of L = 100 mm (i.e. in the direction of U), and its width is the same as the base. Based on the mass of the powder layer in the specified region, M, and the corresponding length, L, the mass flow rate MFR of the feeding process could be calculated as:

$$MFR = \frac{M}{L/U} \tag{1}$$

Four repetitive tests are carried out for each experimental condition. Before each test, the base is carefully cleaned with a brush and vacuum cleaner to ensure no particles remain on the base, and the gap size is examined and calibrated again. To address the effects of feeding conditions on the mass flow rate, a number of experiment tests are carried out. The translational speed U varies from 1 mm/s to 20 mm/s, while the rotational speed ω varies from 10 rpm to 120 rpm.

2.1.2. Experimental materials

To address the effects of particle properties on powder feeding rate, three kinds of powder are used, with properties shown in Table 1 and scanning electron microscope (SEM) images shown in Fig. 3: 1) powder A: pure aluminium powder cut from the wire, the particle shape of which is almost cylinder, with the size of d_p = 0.91 mm; 2) powder B: polyethylene powder, the particle shape of which is irregular, with the size of d_p = 1.25 mm; 3) powder C: aluminium 7075 alloy powder, the shape of which is close to the sphere, with the size of d_p = 0.098 mm. For powder A and powder B, the gap size of δ = 2 mm and δ = 3 mm is used, while for powder C, only the gap size of δ = 1 mm is used. These three kinds of powder have different physical properties, i.e. powder A and powder B have similar particle sizes, but their density and stiffness are much different, while the particle size of powder C is much smaller than that of powder A although they have similar density and stiffness, making the results more representative of the various kinds of powder materials used in reality.

The flowability of powder is characterised by the static repose angle, as shown in Fig. 4 and Table 1, following the same method in Nan et al.

Table 1
Physical properties of powder used in the experiment.

Powder label	Material	Material density (g/cm³)	Volume-based D_{10}, D_{50}, D_{90} (mm)	Static repose angle (°)
Powder A	Pure aluminium	2.70	0.82, 0.91, 1.02	28.6*[a], 35.5*[b]
Powder B	Polyethylene	0.95	1.04, 1.25, 1.59	36.3*[a], 43.6 *[b]
Powder C	7075 aluminium alloy	2.81	0.031, 0.098, 0.21	34.8*[a], 36.3 *[b]

*a: the angle is calculated according to Eq. (2). *b: the angle is calculated according to Eq. (3).
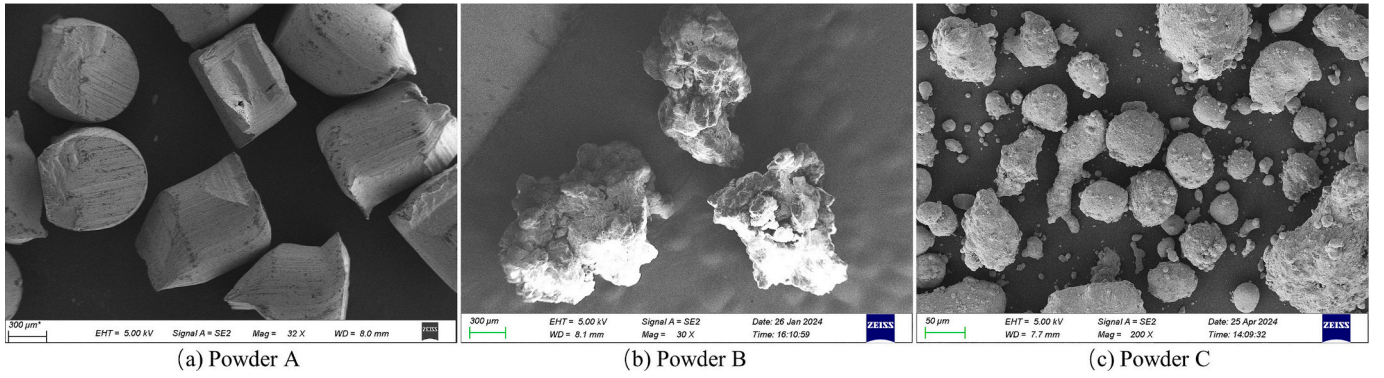
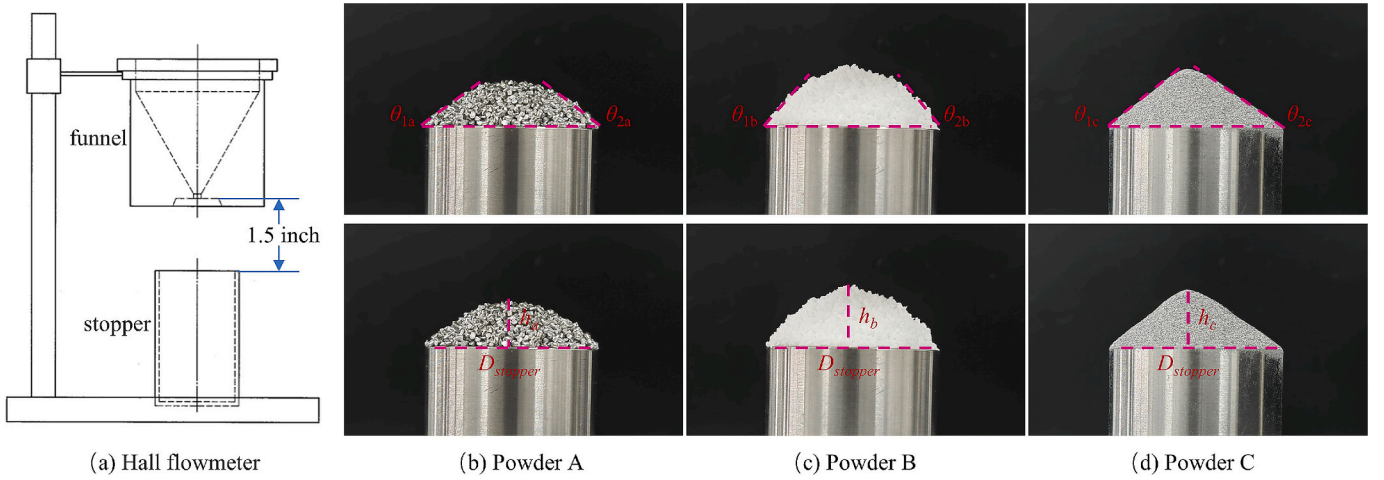Fig. 3. SEM images of particles used in experiments.

Fig. 4. Measurement of the static repose angle of powder used in experiments.

[18]. The diameter of the opening of the fixed funnel is 7.5 mm, 7.5 mm and 2.5 mm for powders A, powder B and powder C, respectively. Both the angle measured from the height of the heap, θ_h, and the angle averaged from the steepest slope of the heap, θ_s, are used here, given as:

$$\theta_h = arctan\left(\frac{2h}{D_{stopper}}\right) \tag{2}$$

$$\theta_s = \frac{\theta_1 + \theta_2}{2} \tag{3}$$

where $D_{stopper}$ is the diameter of the stopper; h is the height of the heap formed on the stopper; θ_1 and θ_2 are the angles measured from the steepest slope of the heap at its left side and right side, respectively. According to the static repose angle, powder B has the worst flowability, while powder C is slightly more cohesive than powder A due to the effect of the particle size.

2.2. Set-up of simulation system

2.2.1. Simulation system and particle properties

The screw-feeding process in the experiment is modelled by Discrete Element Method (DEM), which has been successfully used in the modelling of particle flow in additive manufacturing [19–22], in which particle motion is tracked individually by solving Newton's laws of motion [23,24]. The simulation system in this work is the same as the ones shown in Fig. 2, in which the inner diameter of the funnel is $D_i = 20$ mm while the diameter of the blade and shaft is $D_b = 16$ mm and $D_s = 8$ mm, respectively, and a snapshot of the particle bed at the initial state (t = 0 s) is shown in Fig. 5(a). The physical and mechanical properties of particles used in the simulation are the same as powder A used in the experiment, as summarised in Table 2. The particle size is classified into 10 classes, with the corresponding mass percentage shown in Fig. 5(a). The friction of particles is measured by the sliding method, as detailed described in Nan et al. [25]. The restitution coefficient is measured by tracking the impact process of a single particle against the wall using a high-speed camera, in which the impact velocity and rebound velocity are calculated. If not specified, the interaction parameters of particle-wall are assumed to be the same as that of particle-particle. To speed up the simulation, Young's modulus is scaled down to 1/100 of the realistic value. Meanwhile, only the cases with the translational speed of $U = 10$ mm/s and $U = 20$ mm/s are simulated, while the gap size δ varies from 1 mm to 3.5 mm, and the rotational speed ω varies from 10 rpm to 120 rpm. To examine the particle flow around the screw, two cylindrical cells are used in the analysis of simulation results, as shown in Fig. 5(b), which has the same diameter (i.e. 18 mm) and different heights (cell I: 4 mm, cell II: 8 mm).

2.2.2. Contact model

The contact interaction force of particle against particle/wall is described by the Hertz-Mindlin model [24], in which the normal contact force is given as:

$$F_n = \frac{4E^* a^3}{3R^*} \tag{4}$$

where E^* is the equivalent Young's modulus; R^* is the equivalent radius; a is the contact radius. More details and information on the damping
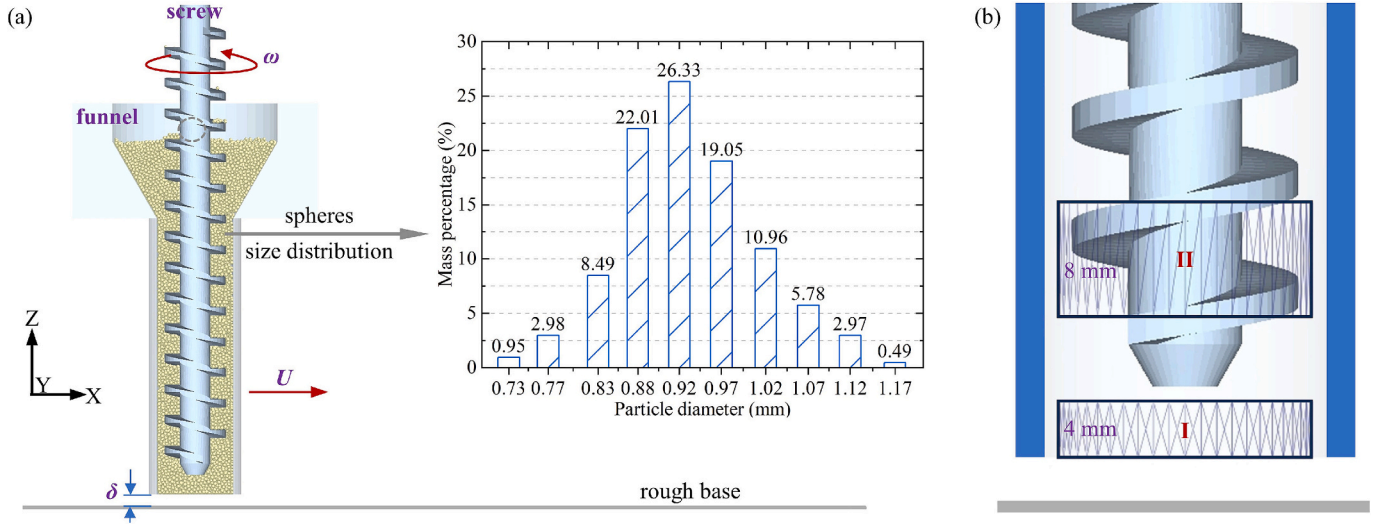
Fig. 5. Schematics of (a) simulation system and corresponding particle size distribution, and (b) two cylindrical cells used in the analysis of simulation results.

Table 2
Physical and mechanical properties of particles used in simulation.

Parameter	Value
Density, ρ_p (kg/m^3)	2700
Young's modulus, E (MPa)	680
Friction coefficient, μ	0.5
Restitution coefficient, e	0.25
Rolling friction coefficient*a, μ_r	0.4

*a: calibrated by tuning the coefficient to get the same dynamic repose angle as the ones measured by the experiment.

force and tangential contact force could be referred to Thorton [24]. To describe the resistance of non-spherical particles to rolling, the rolling friction model developed by Ai et al. [26] is used, in which the total rolling resistance $\boldsymbol{M}_r$ is given as:

$$\boldsymbol{M}_r = \boldsymbol{M}_r^k + \boldsymbol{M}_r^d \tag{5}$$

where $\boldsymbol{M}_r^k$ is the non-viscous term, $\boldsymbol{M}_r^d$ is the viscous term, given as:

$$\boldsymbol{M}_r^k = -\mathrm{k}_r\boldsymbol{\theta}_r \tag{6}$$

$$\left|\boldsymbol{M}_r^k\right| \leq \mu_r R_r F_n \tag{7}$$

$$\boldsymbol{M}_r^d = -2\eta\sqrt{\mathrm{I}_r k_r}\boldsymbol{\omega}_r \tag{8}$$

where θ_r is the relative rotation angle; ω_r is the relative rotational velocity; $R_r = R^*$ is the equivalent rolling radius; I_r is the equivalent moment of inertia for the rotational vibration mode; μ_r is the rolling friction coefficient; η is the rolling viscous damping ratio; k_r is the rolling stiffness, given as:

$$k_r = 3k_n\mu_r^2 R_r^2 \tag{9}$$

where k_n is the normal contact stiffness. It should be noted that the viscous term $\boldsymbol{M}_r^d$ is only applied when the magnitude of the non-viscous term $\boldsymbol{M}_r^k$ is below the limit as defined in Eq. (7). More information could be referred to Ai et al. [26].

2.2.3. Calibration of rolling friction coefficient

Although the particle shape of powder A is angular, as shown in the SEM image in Fig. 3, spherical particles are used in the simulation for simplification, and the effects of shape are modelled by using the rolling friction model described above with a large value of rolling friction
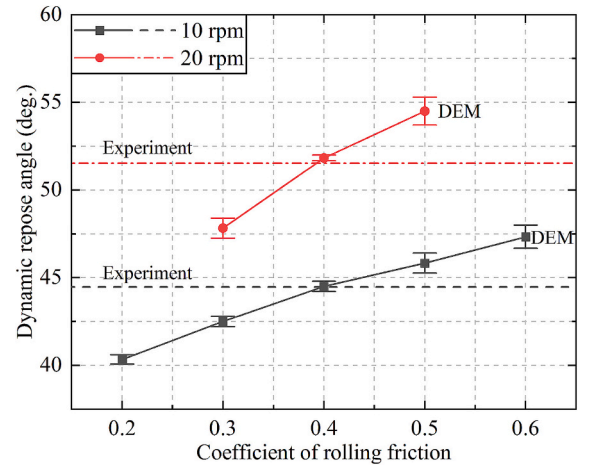

Fig. 6. Calibration of rolling friction coefficient by modelling the dynamic repose angle of powder in a drum with different rotational speeds.
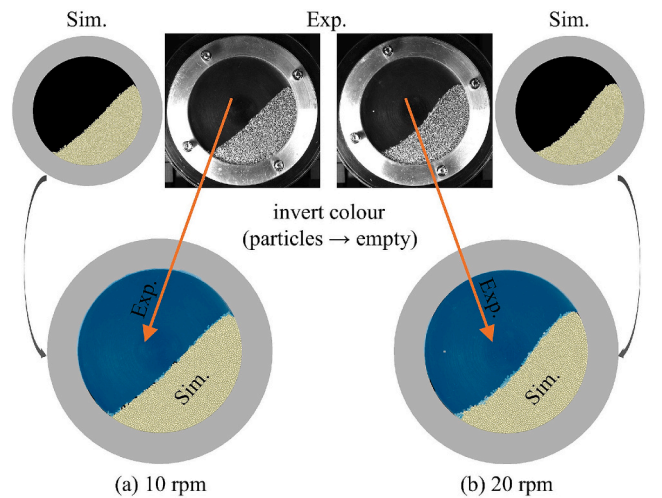

Fig. 7. Validation of rolling friction coefficient of 0.4 used in the simulation by comparing its snapshots of particle heap against the ones tracked by CCD camera in the experiment, for the latter the region with particles (grey colour) is inverted into empty without any colour, while the region without particles (black colour) is inverted into cyan colour for direct comparison with the simulation results. (For interpretation of the references to colour in this figure legend, the reader is referred to the web version of this article.)
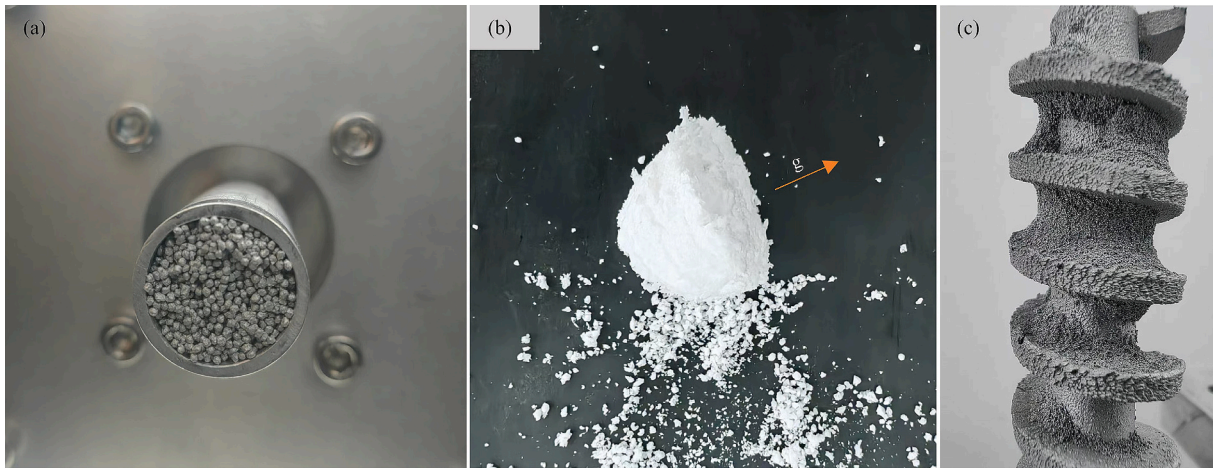
Fig. 8. Examples of particle jamming phenomenon observed in the experiment: (a) powder A, in which the funnel outlet is entirely blocked; (b) powder B, in which the jammed particles form a large lump with a size comparable to the inner diameter of the funnel, and the arrow in orange colour indicates the gravity direction in the feeding process; (c) powder C, in which the particles could be strongly adhered to each other and the walls under the combined effect of the compression of the screw and the heat produced by jamming.

coefficient. To calibrate the rolling friction coefficient used in simulation, the dynamic repose angle of powder A is measured by using an in-house rig and modelled by using DEM with tunning the rolling friction coefficient. In both simulation and experiment, a rotating drum with a diameter of 80 mm and a depth of 10 mm is used, and the total mass of particles in the drum is 25 g, while the repose angle is defined as the angle of the slope of the particle bed in the drum. Two rotational speeds of the drum are used, i.e. 10 rpm and 20 rpm. In the calibration process, the particles have the same physical and mechanical properties as described above. Fig. 6 shows the variation of the dynamic repose angle with the rolling friction coefficient, as obtained from DEM simulation, in which the angle is averaged at different time. It could be found that with the increase of the rolling friction coefficient or the rotational speed of the drum, the dynamic repose angle increases. At both rotational speeds, $\mu_r = 0.4$ could produce the same dynamic repose angle as the experiment. Meanwhile, for the case with $\mu_r = 0.4$, the snapshots of the particle heap are almost entirely overlapped with the ones observed in the experiment, as shown in Fig. 7, which also indicates a good agreement of the packing fraction between the experiment and the simulation case with this rolling friction. Therefore, $\mu_r = 0.4$ is adopted in the simulation to model the effects of shape on particle dynamics in the powder screw-feeding process. It should be noted that there are several simplifications in the simulation, such as using spherical spheres, scaling down Young's modulus and omitting the thermal effects produced by jamming. These would have some effects on the accuracy of the simulation results and capturing all phenomena observed in the experiment, such as surface damage of a few particles, which needs further work in future.

3. Results

3.1. Jamming and blocking

3.1.1. Experimental results

In the screw-feeding process, there is a special phenomenon, i.e. the particles are jammed underneath the screw, and the outlet of the funnel is entirely blocked by these particles. These jammed particles are further compressed by the screw and produce a huge force on the screw, which finally induces the servo motor of the screw to be suddenly stopped during the feeding process. An example of particle jamming during the screw-feeding process is shown in Fig. 8(a). It should be noted that the particle jamming structure would not collapse or disappear if only removing the constrictions of the base. However, if further action is carried out, i.e. rotating the screw clockwise and then anti-clockwise

after re-starting its servo motor, the jamming structure would be destroyed, and all pre-jammed particles are observed to fall out in discrete states, i.e. the same form of powder before the experiment. However, for powder B, the pre-jammed particles falling out of the funnel by destroying the jamming structure using the same method, are in the form of a large lump with a size comparable to the inner diameter of the funnel, as shown in Fig. 8(b). Compared to powder A, powder B is less stiff and thus less resistant to the action of the screw. Therefore, when jamming occurs, the jammed particles are easy to be plastically deformed and compressed into a lump, which would entirely block the outlet of the funnel. This lump could be pushed out the funnel without breakage after re-rotating the screw clockwise and then anti-clockwise and removing the base. It should be noted that the particles in the lump are not consolidated, and the lump could be easily broken into discrete particles after pinching it using fingers. Interestingly, for powder C, under the effect of jamming, the strong interaction between the jammed particles and the geometry walls even produces a large amount of heat, in which the screw is observed to be very warm after the experiment. Under the compression effect of the screw and the jamming-induced heat, the jammed particles are seriously plastically deformed, and they are strongly adhered to each other and the walls, as shown in Fig. 8(c). By knocking down the particles adhered to the screw, it could be inferred that agglomerates in a shape like flat and small chips are formed in the feeding process. Of course, the jammed particles blocking the funnel outlet are still easily to be pushed out by re-rotating the screw clockwise and then anti-clockwise after removing the base.

To examine in which conditions the particles would be jammed, several experimental tests are carried out, and the results are shown in Fig. 9, in which each intersection point of two orange lines represents one test condition in the experiment. The intersection point with a solid symbol or open symbol indicates that the jamming occurs at this test condition, while others indicate that the powder could be successfully fed out of the funnel. Here, only the jamming with extreme strength is included, i.e. the jamming makes the servo motor of the screw stop in the experiment. For powder A and powder B, two gap sizes are used, and 25 kinds of test conditions are examined at each gap size, while for powder C, 16 kinds of test conditions are carried out. As shown in Fig. 9(a), at the gap size of $\delta = 2.0$ mm, there are only 4 kinds of test conditions without jamming, and the feeding process in the other 21 kinds of test conditions is all jammed. At the gap size of $\delta = 3.0$ mm, there are only 13 kinds of test conditions with jamming. It suggests that a narrower clearance between the bottom of the funnel and the top surface of the base is more prone to jamming at the same rotational and translational speeds.
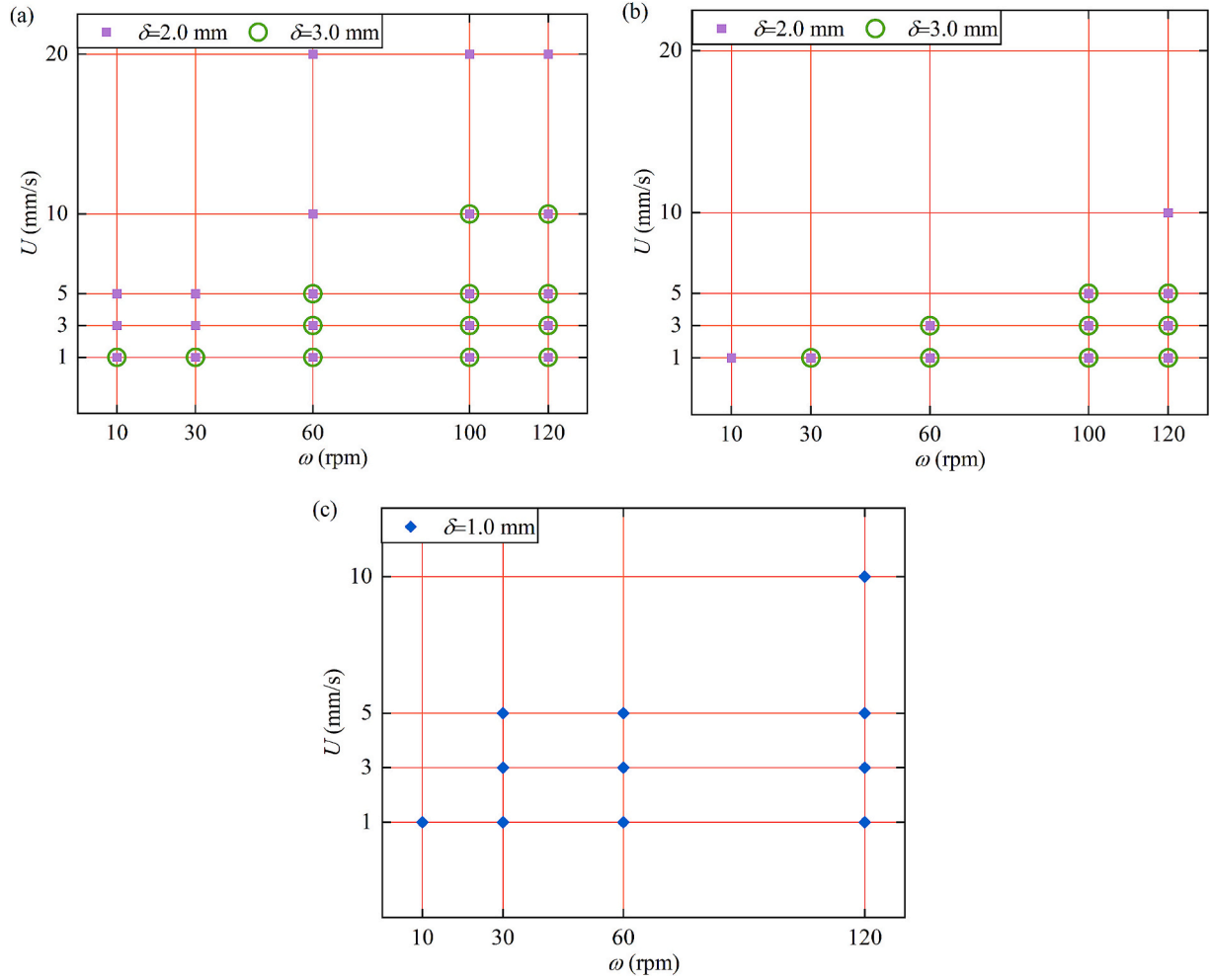
Fig. 9. Jamming map of powder at different rotational speed and translational speed as observed in the experiment: (a) powder A; (b) powder B; (c) powder C; in which the intersection point of two orange lines covered by a solid symbol or open symbol indicates the occurrence of particle jamming at this test condition, while others indicate the successful feeding without jamming, and the data points cover all the experimental conditions at each gap size.
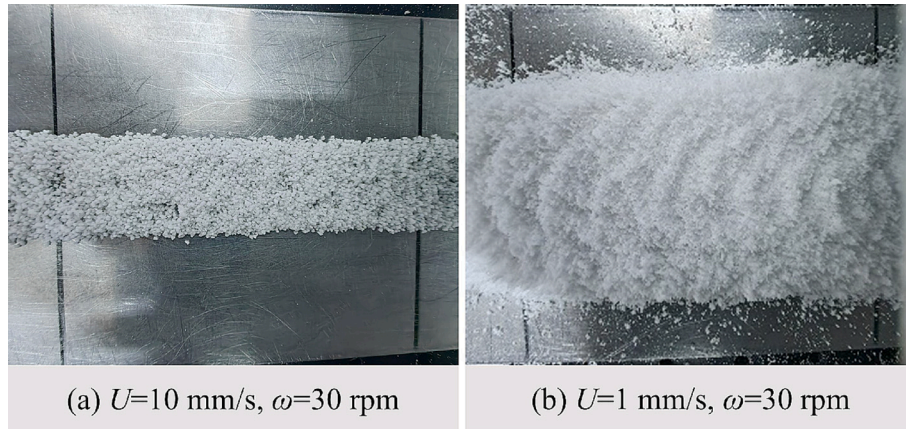

Fig. 10. Experimental snapshots of the layer of powder B formed in the test conditions: (a) without jamming; (b) with jamming, in which an "exploding" styled layer is induced, with the thickness larger than the gap size and the breakage of particles.

Meanwhile, jamming is also more likely to occur when the rotational speed is relatively larger than the translational speed, in which the powder is much over-fed into the funnel outlet. For example, for powder A, at the translational speed of 10 mm/s, the particles would be jammed at $\omega = 100$ rpm, but they could flow at $\omega = 30$ rpm. For powder B, the particles are less stiff than that of powder A, and they are more easily to

be plastically deformed under external force, resulting in less resistance to the motion of the screw. Therefore, the number of test conditions with jamming is less than that of powder A at both gap sizes, which is intuitively expected and observed in Fig. 9(b). For powder C, which has the smallest particle size, the jamming map is similar to that of powder A, indicating that the jamming is less sensitive to particle size.

It should be noted that for powder B, there are 4 kinds of special test conditions at the gap size of 3 mm, i.e. $U = 1$ mm/s and $\omega = 30$ rpm & 60 rpm, $U = 3$ mm/s and $\omega = 60$ rpm, $U = 5$ mm/s and $\omega = 100$ rpm, in which the feeding process is deemed as jamming although the servo motor of the screw is not stopped in the experiment. In these cases, the powder is extruded out of the gap in the form of a loose lump, and then this lump would be broken and "explode" on the base due to the sudden release of the compression force from the screw motion, resulting in an abnormal powder formed on the base. A comparison between the powder layers formed in the test conditions without jamming and with this kind of jamming is shown in Fig. 10. It is clearly found that compared to the normal powder layer, the particles in the abnormal powder are smaller, indicating that particle breakage occurs under the effect of jamming. Meanwhile, the abnormal powder has a much wider width than the normal powder layer. Especially, its thickness is much larger than the gap size, which never exists in the feeding process without jamming.

3.1.2. Simulation results

To explore the underlying mechanism of jamming during the feeding process, the simulation results of powder A are shown below, in which a
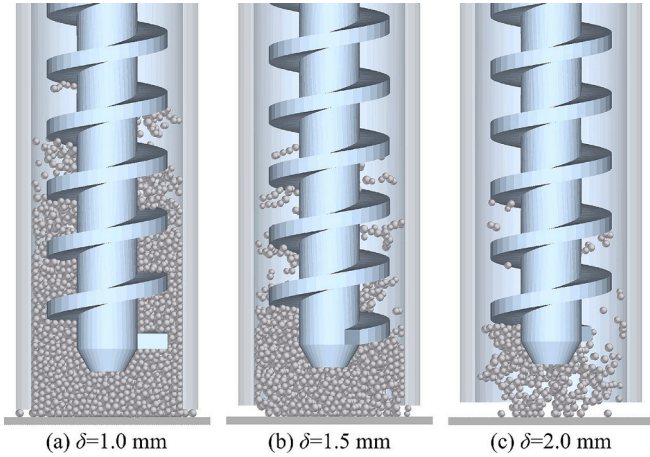
Fig. 11. Snapshots of the spatial distribution particles with compressive force greater than 2 N in the simulation cases with different gap sizes but the same speed ($U = 20$ mm/s and $\omega = 100$ rpm), in which the view with a middle clipping plane is used, and other particles with small compressive force are hidden for better illustration.
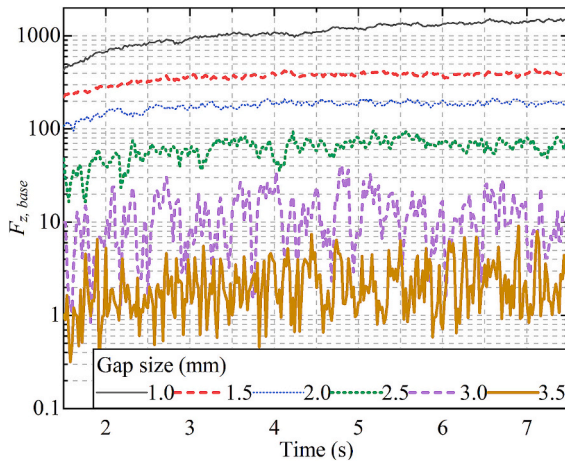
Fig. 12. Variation of the force exerted on the base in the vertical direction with time in the simulation cases with different gap sizes but the same speed ($U = 20$ mm/s and $\omega = 100$ rpm), in which the force is normalised by total particle weight.
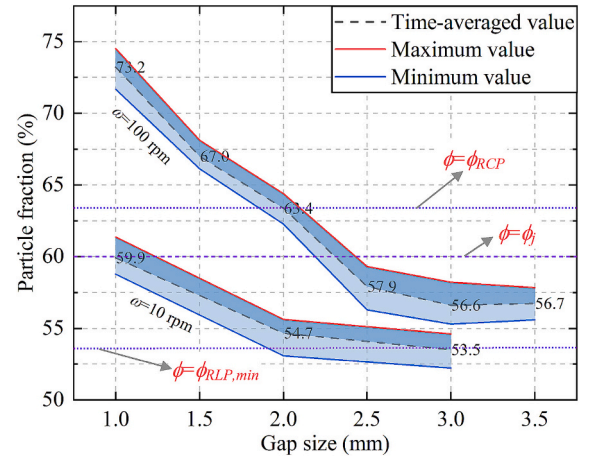
Fig. 13. Particle fraction underneath the screw (i.e. cell I in Fig. 5(b)) for the cases with $U = 20$ mm/s, where $\phi_{RCP} = 0.634$ and $\phi_{RLP} = 0.536$ are theoretical particle fraction at the state random close and loose packing, respectively, and ϕ_j is the theoretical particle fraction at jamming state, above which the particle flow would be jammed.

total of 18 simulation cases are carried out. Fig. 11 shows the snapshots of the spatial distribution of particles with compressive force larger than 2 N, while other particles are hidden for better illustration. It is clearly found that the particles with a large compressive force mainly locate at the region close to the outlet of the funnel, especially underneath the screw. With the increase of gap size, the number of particles with large compressive force decreases significantly. For example, for the case of $\delta = 1.0$ mm, as shown in Fig. 11(a), the particles with large compressive force could even locate in the region with position much higher than the screw bottom, while for the case of $\delta = 2.0$ mm, as shown in Fig. 11(c), there are only a few of particles and they mainly locates in the region with position lower than the screw bottom. These results also suggest that the particles underneath the screw indeed are more prone to be jammed, which agrees well with the experiments shown in Fig. 8. Correspondingly, under the effects of jamming, a large force will be exerted on the geometry. An example is shown in Fig. 12, in which the force is normalised by the total weight of all particles at the initial time (i.e. $t = 0$ s). It could be found that the force exerted on the base is very sensitive to the gap size, increasing sharply as the gap size is reduced. For example, the force could be even about 1000 times the total particle weight for $\delta = 1.0$ mm, while it fluctuates around the total particle weight for $\delta = 3.5$ mm. These results indicate that a very large compressive force between the particle and the particle/wall would be generated when the powder is much over-fed into the gap by the screw, and this interaction force balances the external stress which is used to drive particles to flow, resulting in particle blockage and jamming at the outlet of the funnel.

To further check the state of particle flow underneath the screw, the particle fraction in cell I, as shown in Fig. 5(b), is calculated, which is given as:
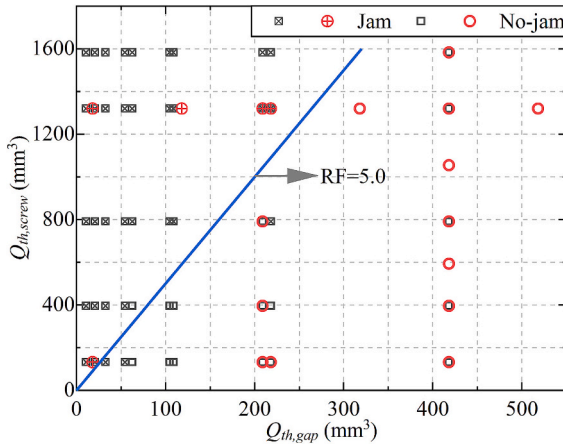
$$\phi = \frac{\sum V_p}{V_{cell}} \tag{10}$$

where V_p is the volume of an individual particle in the cell; V_{cell} is the volume of the cell. Fig. 13 shows the variation of the particle fraction with the gap size, where the time-averaged value and the maximum and minimum values are included. It is clear that at the rotational speed of $\omega = 100$ rpm, the particle fraction decreases with the increase of the gap size, but the extent of the decrease is much reduced when the gap size is larger than 2.5 mm. Especially, at the gap size of $\delta = 1.0$ mm, the time-averaged particle fraction could even be 0.732, much larger than the theoretical particle fraction at random close packing state $\phi_{RCP} = 0.634$.

Table 3
Comparison between the experimental observations and simulation results.

δ (mm)	U (mm/s)	ω (rpm)	Estimated from exp.*	Obtained from sim.	δ (mm)	U (mm/s)	ω (rpm)	Estimated from exp.*	Obtained from sim.
3	10	10	no-jam	no-jam	1	20	100	jammed*	jammed
3	10	30	no-jam	no-jam	1.5	20	100	jammed*	jammed
3	10	60	no-jam	no-jam	2	20	100	jammed	jammed
3	10	100	jammed	jammed	2.5	20	100	not available	no-jam
3	20	10	no-jam	no-jam	3.5	20	100	no-jam*	no-jam
3	20	30	no-jam	no-jam	1	20	10	jammed*	jammed
3	20	45	no-jam*	no-jam	2	20	10	no-jam	no-jam
3	20	60	no-jam	no-jam	3	20	100	no-jam	no-jam
3	20	80	no-jam*	no-jam	3	20	120	no-jam	no-jam

* In the experiment, the jammed state occurs at $\delta = 1$ mm for all values of U and ω used for powder A in this work; for the test conditions used in the experiment, the jammed or no-jammed state is directly described by the results shown in Fig. 9; for the test conditions not used in the experiment (marked by a star), the jammed or no-jammed state could be inferred from the experimental results, i.e. if jammed state occurs at a gap size, for another gap size less than this value, the jammed state would also occur, while if no-jam state occurs at a gap size, for another gap size larger than this value, no-jam state would also occur.

Fig. 14. Variation of $Q_{th,\ screw,\ max}$ with $Q_{th,\ gap}$, where the experimental data (square symbol) and the simulation results (circle symbol) are included.

When the rotational speed is reduced, the particle fraction decreases due to less strength of screw action on the particles. Fig. 13 also shows that the difference in particle fraction between the cases with the different rotational speeds is much reduced as the gap size increases. For example, as the rotational speed decreases from 100 rpm to 10 rpm, the time-averaged particle fraction decreases from 0.732 to 0.599 at the gap size of 1 mm, while it decreases from 0.566 to 0.535 at the gap size of 3 mm. According to the jamming theory of frictional particles [27–29], one indicator of the jamming of dense particle flow is the particle fraction larger than the critical value ϕ_j. Usually, for frictional particles, ϕ_j is less than the particle fraction of random close packing $\phi_{RCP} = 0.634$, but ϕ_j is always larger than the particle fraction of random loose packing ϕ_{RLP}, which has a lowest limit of 0.536. According to the review work of Pan et al. [28], ϕ_j could be roughly estimated as around 0.6 for the particles used in this work. According to this criterion, the judgment of the powder feeding process in a jamming or no-jamming state in simulation is summarised in Table 3, in which the corresponding results of experiments are also included for comparison. It could be found that the simulation results agree well with the one observed in the experiment.

3.1.3. Regime of jamming

Based on the above results, the jamming could be estimated by comparing the theoretic maximum feeding rate of the screw, $Q_{th,\ screw}$ [30,31], and the theoretic requirement of the flow rate of particles from the gap between the funnel and base, $Q_{th,\ gap}$ [25,32], given as:

$$Q_{th,screw} = \frac{\pi}{4}\left(D_i^2 - D_s^2\right)\cdot(p\text{-}t_s)\cdot\frac{\omega}{60}\cdot\phi_{th} \tag{11}$$

Table 4
Summary of the critical ratio of flow rate.

Powder label	Powder A	Powder B	Powder C
$Q_{th,\ screw}/Q_{th,\ gap}$	5.0	15.1	8.8

$$Q_{th,gap} = U_{particle}\cdot\left(\delta - d_p\right)\cdot D_i\cdot\phi_{th} \tag{12}$$

$$RF = \frac{Q_{th,screw}}{Q_{th,gap}} \tag{13}$$

where D_i and D_s are the inner diameter of the funnel and the diameter of the shaft of the screw, respectively; p is the pitch of the screw; t_s is the thickness of the blade of the screw; ω is in the unit of rpm; ϕ_{th} is the particle fraction, which is assumed to be 0.5 for reference in this work; $U_{particle}$ is the mean particle velocity flowing out the gap between the funnel and base, which is assumed to be the same as the translational velocity U of the feeding system for simplification; $\delta - d_p$ is the effective gap size, considering the wall effect [25,32]. Fig. 14 shows the variation of $Q_{th,\ screw}$ with $Q_{th,\ gap}$ for powder A, where both the experimental data and simulation results are included with a total of 70 data points. It is clearly found that jamming tends to occur if the ratio $RF = Q_{th,\ screw}/Q_{th,\ gap}$ is larger than a critical value, and the boundary between jam and no-jam state is well fitted by $RF = 5.0$ with a confidence of 94.3 % (i.e. 4 data points of 70 data points is fit into wrong states). A similar trend is also observed for powder B and powder C, with the corresponding critical value of RF summarised in Table 4, in which the confidence is 92.0 % and 93.7 %, respectively. It should be noted that for powder B, the particles are easy to be plastically deformed and less resistant to the screw motion, especially when the powder is over-fed, resulting in less possibility of the occurrence of jamming. Thus, the critical ratio of the flow rate of powder B is much larger than that of powder A and powder C. Meanwhile, compared to powder A, the particle shape of powder C is closer to spheres, and powder C also has a smaller size, resulting in a slightly larger value of critical ratio of flow rate. Totally, for particles with enough stiffness, the jamming would largely occur if the flow rate ratio given in Eqs. (11)–(13) is larger than 10. Of course, a larger value could be used if the particles are easy to be deformed during the screw-feeding process.

3.2. Mass flow rate

3.2.1. Experimental results

For the cases without jamming, the screw-feeding process could work successfully and smoothly. Based on Eq. (1), the mass flow rate in the experiment could be easily obtained through the mass of the powder layer, and it is further divided by the inner cross-section area of the
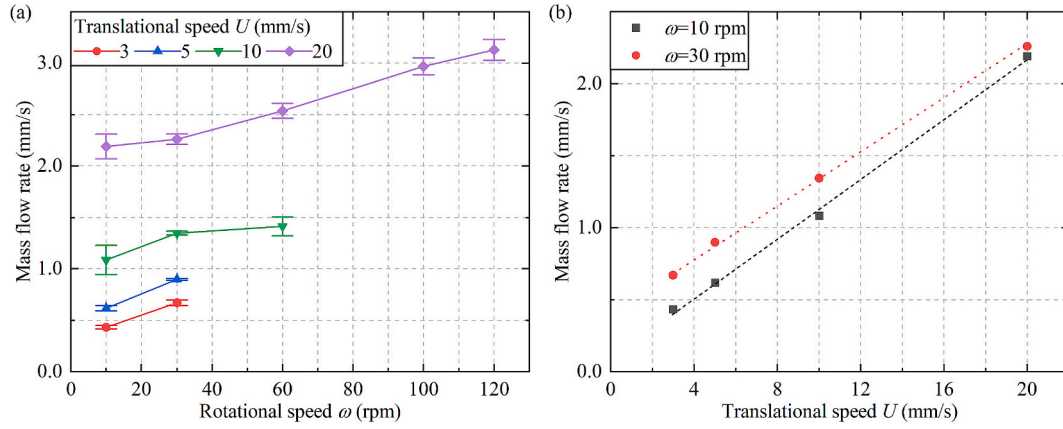
Fig. 15. Variation of the mass flow rate (defined in Eq. (14)) of powder A with (a) rotational speed and (b) translational speed at the gap size of $\delta = 3$ mm in the experiment.
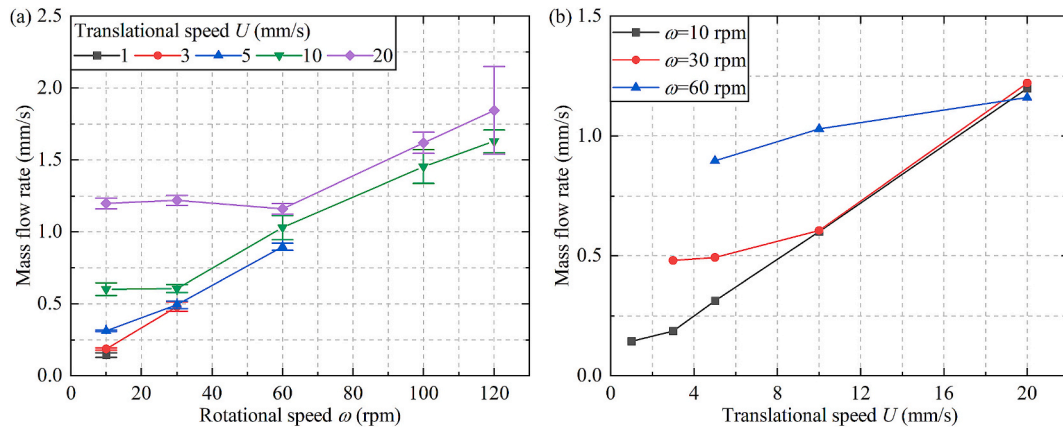

Fig. 16. Variation of the mass flow rate (defined in Eq. (14)) of powder B with (a) rotational speed and (b) translational speed at the gap size of $\delta = 3$ mm in the experiment.

funnel, given as:

$$NMFR = \frac{MFR}{\frac{\pi}{4}\rho_p \left(D_i^2 - D_s^2\right)} \tag{14}$$

Fig. 15 shows the mass flow rate under different test conditions for powder A. It could be found that unlike traditional screw conveying systems [30,31], the mass flow rate in this work not only depends on the

rotational speed of the screw, ω, but also is significantly affected by the translational speed of the feeding system, U.

The mass flow rate is not always linear to the rotational speed ω, as shown in Fig. 15(a). For example, with the increase of rotational speed, the mass flow rate at $U = 20$ mm/s first increases slowly, and then it begins to increase almost linearly. This trend is more significant for power B, as shown in Fig. 16(a). At the translational speed of 5 mm/s, the mass flow rate of powder B almost increases linearly with the
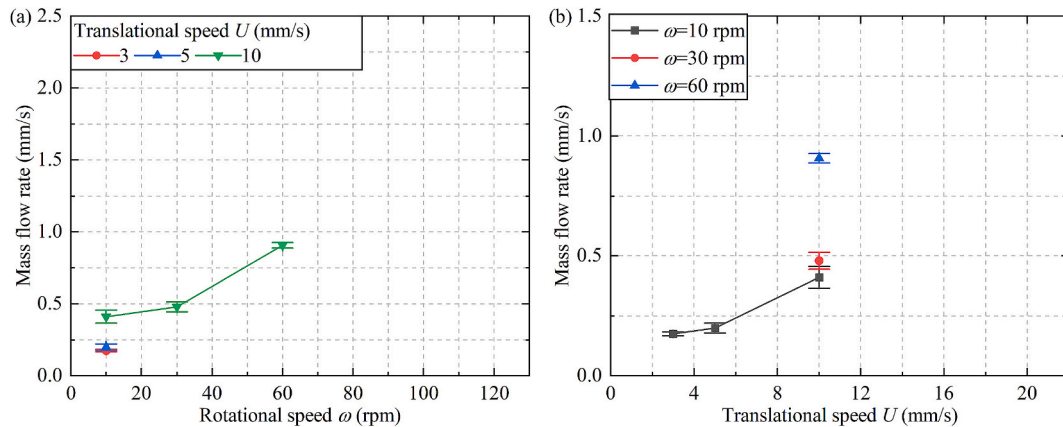

Fig. 17. Variation of the mass flow rate (defined in Eq. (14)) of powder C with (a) rotational speed and (b) translational speed at the gap size of $\delta = 1$ mm in the experiment.
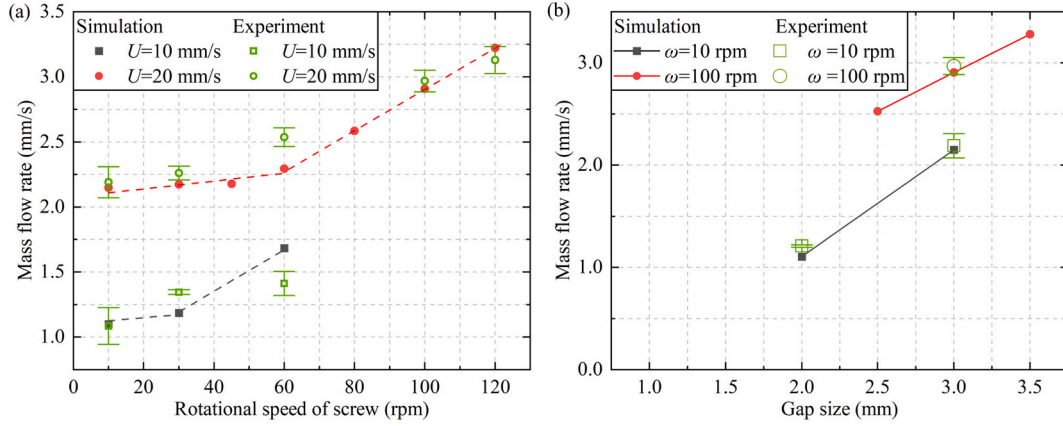
Fig. 18. Variation of the time-averaged mass flow rate (defined in Eq. (14)) with (a) the rotational speed at the gap size of 3 mm and (b) the gap size at the translational speed of 20 mm/s, where the corresponding results are also included for comparison.

rotational speed before the occurrence of jamming. However, as the translational speed rises to 10 mm/s and beyond, with the increase of rotational speed, the mass flow rate of powder B first shows a plateau, and then it increases almost linearly. These results indicate that there is a critical rotational speed, less than which the rotational speed would have less effect on the mass flow rate than the translational speed. It is also found that this critical rotational speed is not constant, and it increases with the translational speed. For example, as shown in Fig. 16 (a), the critical rotational speed is 30 rpm at the translational speed of 10 mm/s, while it increases to 60 rpm at the translational speed of 20 mm/s.

On the other hand, as shown in Fig. 15(b), with the increase of translational speed, a linear increase of mass flow rate is observed for powder A. However, this linear trend is only observed at large translational speed for powder B, the underlying mechanism of which is not known and needs further research work in future. For powder C, as shown in Fig. 17, with the increase of rotational speed or translational speed, the mass flow rate shows a similar trend as observed for powders A and powder B.

3.2.2. Simulation results

On the other hand, the time-averaged mass flow rate, as obtained from DEM simulation, is shown in Fig. 18, in which only the cases without jamming are included. The corresponding experimental data is also included to validate the simulation results. As shown in Fig. 18(a), it could be found that at both translational speeds (i.e. 20 mm/s and 10

mm/s), the simulation data shows a good agreement with the ones obtained in the experiment at different rotational speeds. The average absolute relative error (i.e. *AARE*) is 6.45 %, which is given as:

$$AARE = \frac{1}{N} \sum_{i=1}^{N} \left| \frac{NMFR_{sim,i} - NMFR_{exp,i}}{NMFR_{exp,i}} \right| \qquad (15)$$

where $N = 8$ is the total number of experimental data shown in Fig. 18 (a). Meanwhile, with the increase of the rotational speed, the mass flow rate first increases slowly, then increases almost linearly when the rotational speed goes beyond the critical value. Fig. 18(a) also shows that this critical rotational speed has a larger value at the larger translational speed. These trends all agree well with the observations in Fig. 15-Fig. 17. On the other hand, it can be found that the mass flow rate is also sensitive to the gap size, as shown in Fig. 18(b). With the increase of gap size, the mass flow rate increases almost linearly. Meanwhile, the simulation results agree well with the experimental data, and the corresponding *AARE* is only 4.04 %.

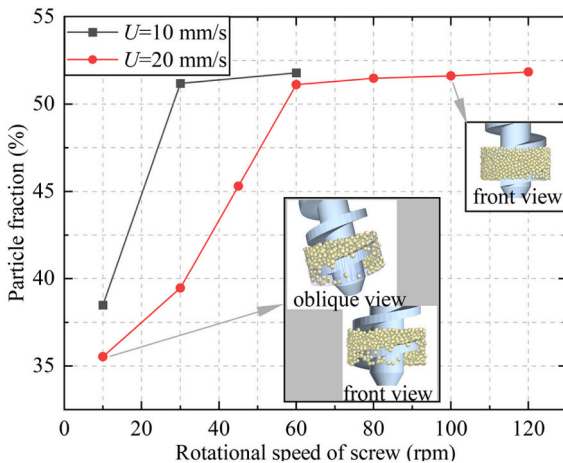To examine the underlying mechanism of the variation of mass flow

Fig. 19. Variation of the packing fraction in cell II (as shown in Fig. 5(b)) with the rotational speed at the gap size of 3 mm, as obtained from DEM simulation.
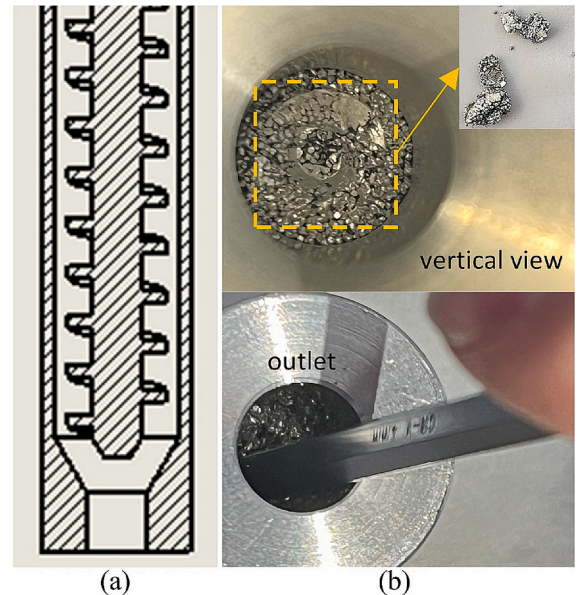

Fig. 20. Jamming phenomenon observed for the funnel with a contracting outlet, which is used in the early stage of the set-up of the experiment rig: (a) schematics of the funnel; (b) the contracting outlet is entirely blocked by the consolidated powder due to the jamming; (c) the funnel could not be cleaned by using hands from its bottom.
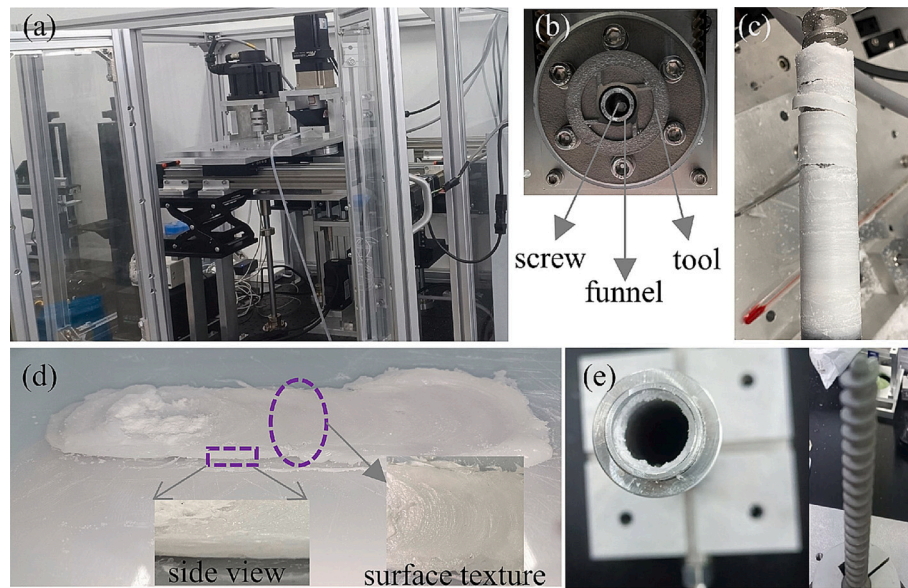
Fig. 21. Powder-based additive friction stir deposition manufacturing: (a) snapshot of rig; (b) assembly of the screw, funnel and tool; (c) material return due to over-feeding at large rotational speed of the screw; (d) final product with a thickness of around 5 mm manufactured from powder B; (e) snapshot of the funnel and screw after experiment, in which no powder is adhered to the walls and the outlet of funnel is not blocked.

rate with the rotational speed, the packing fraction around the last pitch of the screw, i.e. cell II shown in Fig. 5(b), is calculated by using Eq. (10). As shown in Fig. 19, at a low rotational speed, the particle fraction is much less than that at a large rotational speed. For example, at $U = 20$ mm/s, the packing fraction is only 35.5 % at $\omega = 10$ rpm, and it increases to around 51 % when the rotational speed increases beyond 60 rpm. It indicates that the pitch of the screw is not well filled by particles at low rotational speed, which could be also clearly observed from the snapshots of particles in cell II, as shown in Fig. 19. With the increase of rotational speed, at both translational speeds, the particle fraction firstly increases and then approaches to a plateau. Surprisingly, the critical rotational speed obtained from the particle fraction is the same as the ones obtained from the mass flow rate by comparing the simulation data in Fig. 18(a) and Fig. 19. It indicates that at low rotational speed, the contribution of increasing rotational speed is mainly compressing the bulk particles around the screw into a denser state. Under this condition, the mass flow rate primarily depends on the translational speed, resulting in no significant increase in the mass flow rate if only the rotational speed is increased. When the rotational speed is beyond the critical value, in which the packing fraction reaches a limit, the contribution of increasing rotational speed turns to feed more powder into the gap between the funnel and base. Under this condition, the mass flow rate is almost linear to the rotational speed.

4. Discussions

In the early stage of the set-up of the experimental rig, the funnel with a contracting outlet is first considered, as shown in Fig. 20(a), and powder A is used for trial tests. However, the experimental results show that particle jamming can easily occur in this kind of funnel. For example, using the same test conditions as the ones in Fig. 9(a), there are only three kinds of test conditions without the occurrence of jamming, i. e. $U = 10$ mm/s & $U = 20$ mm/s at $\omega = 10$ rpm and $\delta = 3$ mm, $U = 20$ mm/s at $\omega = 30$ rpm and $\delta = 3$ mm, while the screw-feeding process in other kinds of test conditions is all jammed. Meanwhile, these jamming structures could not be easily destroyed by using the method described above, i.e. removing the base, rotating the screw clockwise and later anticlockwise. Under this situation, the screw needs to be pulled out after removing the base, and then a metal rod is inserted into and out of the funnel several times to destroy the jammed structure. Especially if

increasing the rotational speed beyond the ones used above, such as $\omega = 200$ rpm, a very strong jamming is observed to be formed at the contraction, in which a large amount of heat is generated, resulting in powder consolidation at this region. An example is shown in Fig. 20(b), in which the entirely blocked funnel could be only cleaned from its bottom by using a drill.

On the other hand, the powder feeding rate is important for manufacturing the final product in AFSD. Here, a trial test is carried out for powder B, as shown in Fig. 21. An image of the experimental rig is shown in Fig. 21(a), and the assembly of the screw, funnel and tool is shown in Fig. 21(b). Inappropriate rotational speed of the screw would lead to unsuccessful manufacturing of the product, even in the cases without the jamming described above. For example, too large rotational speed would lead to the over-feeding of powder to some extent, and it would make the softened material return upwards and enwrap the screw, as shown in Fig. 21(c), which finally results in no powder feeding into the tool region and the failure of the manufacturing process. On the contrary, the appropriate rotational speed of the screw would lead to the successful manufacturing of the product. An example is the plate manufactured from powder B, as shown in Fig. 21(d), which has a thickness of around 5 mm and a surface without large roughness. Meanwhile, after the manufacturing process, it could be observed that there is no powder adhered to the screw tip, and the funnel is in a good state, in which the outlet is not blocked or adhered by a large amount of powder. Further details of the manufactured product in AFSD will be described in another work in future.

5. Conclusions

In this work, the screw-feeding process in powder-based additive friction stir deposition (AFSD) is analysed in this work, in which the screw is only used to feed powder while the friction-induced heat and plastic deformation of particles is mainly contributed by the high-speed rotating tool. The effect of feeding conditions on the particle jamming problem, which should be avoided in the manufacturing process, and the feeding rate, which is quantified by the mass flow rate of particles flowing out the funnel, is explored through experiment and numerical simulation using Discrete Element Method (DEM). The primary findings can be summarised as follows:

1) Particle jamming would entirely block the funnel outlet and produce a huge force on the screw, even resulting in the stop of the screw motor. A narrow gap between the funnel outlet and the base is prone to particle jamming. Jamming is also sensitive to the design of the funnel outlet, and a contracting outlet would make the jamming problem more serious, in which a large amount of heat is generated, even resulting in powder consolidation at this region.

2) Jamming is more likely to occur when the rotational speed is relatively larger than the translational speed, in which the powder would be much over-fed by the screw. The simulation results agree well with experiments in terms of the locations of jamming and the judgment of the occurrence of jamming at specified feeding conditions. A mathematical model to predict the critical rotational speed above which the particle jamming would occur is proposed.

3) For the feeding conditions without jamming, the feeding rate not only depends on the rotational speed of the screw but also is significantly affected by the translational speed. The feeding rate is not always linear to the rotational speed, and the underlying reason is due to the low particle fraction at low rotational speed.

4) There is a critical rotational speed, less than which the feeding rate is more dominated by the translational speed and gap, and above which the feeding rate is linear to the rotational speed until the occurrence of jamming. This critical rotational speed increases with the translational speed. The simulation results agree well with the experiments in terms of the feeding rate at different feeding conditions, with an average absolute relative error of less than 6.5 %.

CRediT authorship contribution statement

Wenguang Nan: Writing – review & editing, Writing – original draft, Visualization, Validation, Supervision, Methodology, Investigation, Formal analysis, Data curation. **Wenbin Xuan:** Visualization, Investigation, Formal analysis, Data curation. **Ziming He:** Investigation, Data curation. **Haimeng Hou:** Methodology. **Zhonggang Sun:** Supervision. **Wenya Li:** Supervision.

Declaration of competing interest

The authors declare that they have no known competing financial interests or personal relationships that could have appeared to influence the work reported in this paper.

Acknowledgements

Data availability

Data will be made available on request.

References

[1] J.B. Jordon, P.G. Allison, B.J. Phillips, D.Z. Avery, R.P. Kinser, L.N. Brewer, C. Cox, K. Doherty, Direct recycling of machine chips through a novel solid-state additive manufacturing process, Mater. Des. 193 (2020).

[2] L.P. Martin, A. Luccitti, M. Walluk, Repair of aluminum 6061 plate by additive friction stir deposition, Int. J. Adv. Manuf. Technol. 118 (2021) 759–773.

[3] L.P. Martin, A. Luccitti, M. Walluk, Evaluation of additive friction stir deposition of AISI 316L for repairing surface material loss in AISI 4340, Int. J. Adv. Manuf. Technol. 121 (2022) 2365–2381.

[4] A. Mukhopadhyay, P. Saha, A critical review on process metrics–microstructural evolution–process performance correlation in additive friction stir deposition (AFS-D), J. Braz. Soc. Mech. Sci. Eng. 44 (2022).

[5] R.S. Mishra, R.S. Haridas, P. Agrawal, Friction stir-based additive manufacturing, Sci. Technol. Weld. Join. 27 (2022) 141–165.

[6] D.D. Gu, W. Meiners, K. Wissenbach, R. Poprawe, Laser additive manufacturing of metallic components: materials, processes and mechanisms, Int. Mater. Rev. 57 (2013) 133–164.

[7] N. Shamsaei, A. Yadollahi, L. Bian, S.M. Thompson, An overview of direct laser deposition for additive manufacturing; Part II: Mechanical behavior, process parameter optimization and control, Addit. Manuf. 8 (2015) 12–35.

[8] S.S. Joshi, S.M. Patil, S. Mazumder, S. Sharma, D.A. Riley, S. Dowden, R. Banerjee, N.B. Dahotre, Additive friction stir deposition of AZ31B magnesium alloy, J. Magn. Alloys 10 (2022) 2404–2420.

[9] M.E.J. Perry, R.J. Griffiths, D. Garcia, J.M. Sietins, Y. Zhu, H.Z. Yu, Morphological and microstructural investigation of the non-planar interface formed in solid-state metal additive manufacturing by additive friction stir deposition, Addit. Manuf. 35 (2020).

[10] S. Sharma, K.V. Mani Krishna, M. Radhakrishnan, M.V. Pantawane, S.M. Patil, S.S. Joshi, R. Banerjee, N.B. Dahotre, A pseudo thermo-mechanical model linking process parameters to microstructural evolution in multilayer additive friction stir deposition of magnesium alloy, Mater. Des. 224 (2022).

[11] H. Chen, X. Meng, J. Chen, Y. Xie, J. Wang, S. Sun, Y. Zhao, J. Li, L. Wan, Y. Huang, Wire-based friction stir additive manufacturing, Addit. Manuf. 70 (2023).

[12] S.C. Beck, C.J. Williamson, R.P. Kinser, B.A. Rutherford, M.B. Williams, B.J. Phillips, K.J. Doherty, P.G. Allison, J.B. Jordon, Examination of microstructure and mechanical properties of direct additive recycling for Al-mg-Mn alloy machine chip waste, Mater. Des. 228 (2023).

[13] A. Mukhopadhyay, P. Saha, Mechanical and microstructural characterization of aluminium powder deposit made by friction stir based additive manufacturing, J. Mater. Process. Technol. 281 (2020).

[14] B. Chaudhary, N.K. Jain, J. Murugesan, Development of friction stir powder deposition process for repairing of aerospace-grade aluminum alloys, CIRP J. Manuf. Sci. Technol. 38 (2022) 252–267.

[15] H. Aghajani Derazkola, F. Khodabakhshi, A.P. Gerlich, Friction-forging tubular additive manufacturing (FFTAM): a new route of solid-state layer-upon-layer metal deposition, J. Mater. Res. Technol. 9 (2020) 15273–15285.

[16] H. Aghajani Derazkola, F. Khodabakhshi, A.P. Gerlich, Fabrication of a nanostructured high strength steel tube by friction-forging tubular additive manufacturing (FFTAM) technology, J. Manuf. Process. 58 (2020) 724–735.

[17] T. Bor, M.D. Leede, F. Deunk, J. Lind, W. Lievestro, H.-J. Smit, R. Ariës, V. Dolas, N. Helthuis, M. Luckabauer, R. Akkerman, Friction screw extrusion additive manufacturing of an Al-Mg-Si alloy, Addit. Manuf. 72 (2023).

[18] W. Nan, M. Pasha, U. Zafar, S. Nadimi, W.P. Goh, M. Ghadiri, Characterisation of gas-atomised metal powders used in binder jet 3D printing, Powder Technol. 436 (2024).

[19] S. Zinatlou Ajabshir, C. Hare, D. Sofia, D. Barletta, M. Poletto, Investigating the effect of temperature on powder spreading behaviour in powder bed fusion additive manufacturing process by Discrete Element Method, Powder Technol. (2024) 436.

[20] S. Haeri, Y. Wang, O. Ghita, J. Sun, Discrete element simulation and experimental study of powder spreading process in additive manufacturing, Powder Technol. 306 (2016) 45–54.

[21] M.Y. Shaheen, A.R. Thornton, S. Luding, T. Weinhart, The influence of material and process parameters on powder spreading in additive manufacturing, Powder Technol. 383 (2021) 564–583.

[22] J. Zhang, Y. Tan, X. Xiao, S. Jiang, Comparison of roller-spreading and blade-spreading processes in powder-bed additive manufacturing by DEM simulations, Particuology 66 (2022) 48–58.

[23] P.A. Cundall, O.D.L. Strack, A discrete numerical model for granular assemblies, Geotechnique 29 (1979) 47–65.

[24] C. Thornton, Granular Dynamics, Contact Mechanics and Particle System Simulations: A DEM Study, 2015.

[25] W. Nan, M. Pasha, B. Tina, L. Alejandro, Z. Umair, N. Sadegh, M. Ghadiri, Jamming during particle spreading in additive manufacturing, Powder Technol. 338 (2018) 253–262.

[26] J. Ai, J.-F. Chen, J.M. Rotter, J.Y. Ooi, Assessment of rolling resistance models in discrete element simulations, Powder Technol. 206 (2011) 269–282.

[27] S. Luding, So much for the jamming point, Nat. Phys. 12 (2016) 531–532.

[28] D. Pan, Y. Wang, H. Yoshino, J. Zhang, Y. Jin, A review on shear jamming, Phys. Rep. 1038 (2023) 1–18.

[29] P. Wang, C. Song, Y. Jin, H.A. Makse, Jamming II: Edwards' statistical mechanics of random packings of hard spheres, Physica A 390 (2011) 427–455.

[30] D. Minglani, A. Sharma, H. Pandey, R. Dayal, J.B. Joshi, S. Subramaniam, A review of granular flow in screw feeders and conveyors, Powder Technol. 366 (2020) 369–381.

[31] A.W. Roberts, The influence of granular vortex motion on the volumetric performance of enclosed screw conveyors, Powder Technol 104 (1999) 56–67.

[32] W.G. Nan, M. Ghadiri, Numerical simulation of powder flow during spreading in additive manufacturing, Powder Technol. 342 (2019) 801–807.